

Power-function expansion of the nondimensional complementary relationship of evaporation: the emergence of dual attractors

Jozsef Szilagyi¹, Ning Ma², Richard D Crago³, and Russell J. Qualls⁴

¹University of Nebraska/Budapest University of Technology and Economics

²Institute of Geographic Sciences and Natural Resources Research, Chinese Academy of Sciences

³Bucknell University

⁴University of Idaho

November 22, 2022

Abstract

The polynomial form of the nondimensional complementary relationship (CR) follows from an isenthalpic process of evaporation under a constant surface available energy and unchanging wind. The exact polynomial expression results from rationally derived first and second-order boundary conditions (BC). By keeping the BCs, the polynomial can be extended into a two-parameter (a and b) power function for added flexibility. When $a = b = 2$ it reverts to the polynomial version. With the help of Australian FLUXNET data it is demonstrated that the power-function formulation excels among CR-based two-parameter models considered, even when $a = 2$ is prescribed to reduce the number of parameters to calibrate to two. The same power-function approach ($a = 2$) is then employed with a combination of different gridded monthly potential evaporation terms across Australia, while calibrating b against the multiyear simplified water-balance evaporation rate on a cell-by-cell basis. The resulting bi-modal histogram of the b values peaks first near $b = 2$ and then at $b - 1$ (secondary modus), confirming earlier findings that occasionally a linear version (i.e., $b = 1$) of the CR yields the best estimates. It is further demonstrated that the linear form emerges when regional-scale transport of moist air is negligible toward the study area during its drying, while the more typical nonlinear CR version prevails otherwise. A thermodynamic-based explanation is yet to be found as to why the flexible power function curves (i.e., $b \in [2, \infty)$) converge to the polynomial one ($b = 2$) in such cases.

1 **Power-function expansion of the nondimensional complementary relationship of**
2 **evaporation: the emergence of dual attractors**

3 Jozsef Szilagyi^{a,b,*}, Ning Ma^c, Richard D. Crago^d, Russell J. Qualls^e

4 ^aDepartment of Hydraulic and Water Resources Engineering, Budapest University of
5 Technology and Economics, Muegyetem Rkp. 1-3, Budapest, Hungary, H-1111

6 ^bConservation and Survey Division, School of Natural Resources, University of Nebraska-
7 Lincoln, 3310 Holdrege St., Lincoln, Nebraska, USA

8 ^cKey Laboratory of Water Cycle and Related Land Surface Processes, Institute of Geographic
9 Sciences and Natural Resources Research, Chinese Academy of Sciences, Beijing, China

10 ^dDepartment of Civil and Environmental Engineering, Bucknell University, Lewisburg,
11 Pennsylvania, USA

12 ^eDepartment of Chemical and Biological Engineering, University of Idaho, Moscow, Idaho, USA

13 *Corresponding author, e-mail: szilagyi.jozsef@emk.bme.hu

14

15 **Key points**

16 i) The power-function extension of the polynomial complementary relationship (CR) of
17 evaporation can account for horizontal moisture advection

18 ii) Under negligible advection an existing linear version of the nondimensional CR is recaptured

19 iii) The power-function solution converges to the existing polynomial CR otherwise

20 **Abstract** The polynomial form of the nondimensional complementary relationship (CR) follows
21 from an isenthalpic process of evaporation under a constant surface available energy and
22 unchanging wind. The exact polynomial expression results from rationally derived first and
23 second-order boundary conditions (BC). By keeping the BCs, the polynomial can be extended
24 into a two-parameter (a and b) power function for added flexibility. When $a = b = 2$ it reverts to
25 the polynomial version. With the help of Australian FLUXNET data it is demonstrated that the
26 power-function formulation excels among CR-based two-parameter models considered, even
27 when $a = 2$ is prescribed to reduce the number of parameters to calibrate to two. The same
28 power-function approach ($a = 2$) is then employed with a combination of different gridded
29 monthly potential evaporation terms across Australia, while calibrating b against the multiyear
30 simplified water-balance evaporation rate on a cell-by-cell basis. The resulting bi-modal
31 histogram of the b values peaks first near $b = 2$ and then at $b \rightarrow 1$ (secondary modus), confirming
32 earlier findings that occasionally a linear version (i.e., $b = 1$) of the CR yields the best estimates.
33 It is further demonstrated that the linear form emerges when regional-scale transport of moist air
34 is negligible toward the study area during its drying, while the more typical nonlinear CR version
35 prevails otherwise. A thermodynamic-based explanation is yet to be found as to why the flexible
36 power function curves (i.e., $b \neq 2$) converge to the polynomial one ($b = 2$) in such cases.

37 1. Introduction

38 The complementary relationship (CR) of evaporation is a powerful tool [see the latest global
39 studies by *Ma et al. (2021)*, *Brutsaert et al. (2020)*] for predicting actual land evaporation (E)
40 rates with the help of basic meteorological variables (i.e., air temperature, humidity, net surface
41 radiation and wind speed) all obtained at a single elevation above the ground. Since its original
42 formulation by *Bouchet (1963)*, it has evolved into various versions [see *Han & Tian (2020)* for
43 a brief overview] based on different heuristic arguments.

44 After almost six decades of the groundbreaking study by *Bouchet (1963)*, *Szilagyi (2021)* as well
45 as *Crago & Qualls (2021)* gave the CR a stronger physical foundation following the lead of
46 *Monteith (1981)* who first defined the thermodynamic pathway a parcel of air near the
47 evaporating drying surface must follow under unchanging wind conditions and constant
48 available energy (Q_n) at the surface during an adiabatic and isobaric (thus, isenthalpic) process.

49 *Crago & Qualls (2021)*, *Szilagyi (2021)* extended the study of *Monteith (1981)* by considering a
50 full wet-to-dry cycle and simultaneously tracing the state of the air parcel at the land surface in
51 addition to the one near to it (e.g., 2-m above ground). The key to success lies in the estimation
52 of the wet surface temperature (T_{ws}) from typical drying (i.e., not completely wet) environmental
53 measurements for anchoring the surface isenthalp to the saturation vapor pressure curve in the
54 state diagram.

55 With the help of the two isenthalps, *Qualls & Crago (2020)* graphically illustrated evaporation
56 from saturated surfaces. Using a similar approach, *Crago & Qualls (2021)* reproduced an
57 existing linear nondimensional formulation of the CR (*Crago & Qualls, 2018*), while *Szilagyi*
58 (*2021*) independently of them and by a different approach reproduced both the existing linear as
59 well as the nonlinear polynomial formulation of the CR (*Szilagyi et al., 2017*), the latter having
60 been originally inspired by the study of *Brutsaert (2015)*.

61 Here a brief summary of this thermodynamical approach is provided. First the nondimensional
62 linear as well as the polynomial CR equations are derived. Then the latter is expanded by a
63 power function formulation to make it more flexible. The resulting power function with two
64 additional parameters (a and b) is to be applied with daily measurements of air temperature (T),
65 pressure (p), vapor pressure deficit (VPD), net radiation (R_n), ground heat conduction (G) and
66 wind speed (u) in addition to eddy-covariance obtained sensible (H) and latent heat (LE) fluxes
67 for validation at seven Australian FLUXNET sites. The resulting E values are then to be
68 compared with similar estimates of three additional CR-based heuristic evaporation methods by
69 *Kahler & Brutsaert (2006)*, *Han & Tian (2012)*, and *Gao & Xu (2021)*, to demonstrate the
70 predictive capability of the power-function approach. All three methods have two parameters to
71 calibrate, similar to the present power-function one, once one of its parameter values (a) is fixed.

72 Finally, the power-function approach is to be applied with 0.25-degree spatial resolution gridded
73 monthly input data after aggregation to 0.5-degree values over Australia and its sole free
74 parameter (b) to be calibrated on a cell-by-cell basis against 0.5-degree simplified water-balance
75 derived evaporation estimates (E_{wb}) to see how its value changes spatially and what may drive
76 those changes.

77 Note that this work is not meant as a calibration/verification analysis of a preferred two-
 78 parameter approach over other existing similar (or single parameter) approaches. That is why the
 79 steps required for such a study (i.e., validation with data separate from calibration, sensitivity
 80 analysis of the parameters, etc.) are deliberately not repeated here, specifically because it would
 81 blur the focus of the present work which is the investigation/demonstration, by the help of a
 82 recently discovered power-function expansion, of how and when the horizontal advection of
 83 humidity over a drying surface produces/affects the thermodynamically-derived linear and
 84 nonlinear forms (Szilagyi, 2021) of the CR of evaporation and the typical environmental
 85 conditions under which, one or the other, emerges.

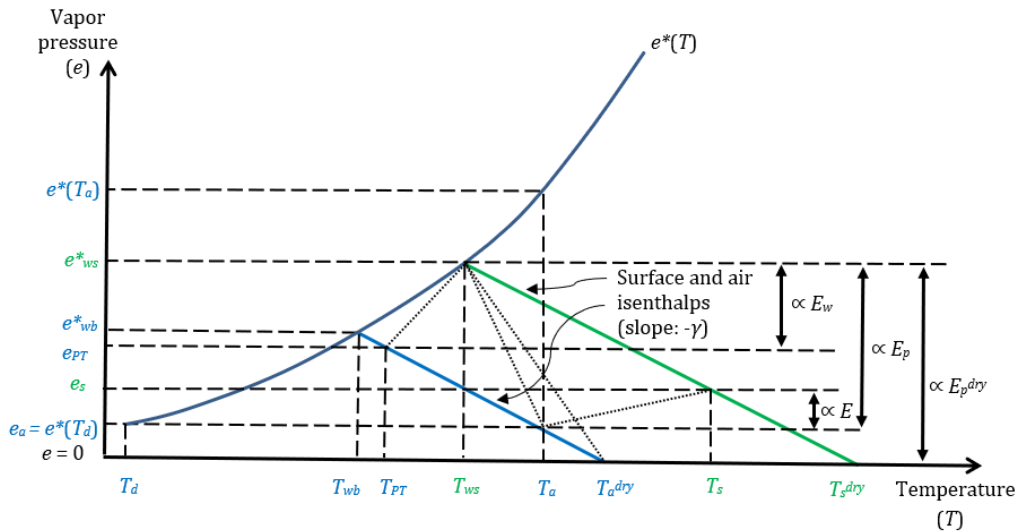
86

87 2. A concise thermodynamical derivation of the nondimensional polynomial 88 complementary relationship

89 During drying out of the environment under unchanging wind conditions, constant pressure as
 90 well as constant available energy, $Q_n (= R_n - G)$ at the surface, the change ($d.$) in vapor pressure
 91 (e) is strictly tied to changes in air temperature (T) near the surface via the equation

$$92 \quad de/dT = -\gamma \quad (1)$$

93 (*Monteith, 1981; Qualls & Crago, 2020, Szilagyi, 2021*). Here $\gamma = c_p p (0.622 L_v)^{-1}$ is the
 94 psychrometric constant, c_p the specific heat of air under constant pressure, and L_v is the latent
 95 heat of vaporization. Eq. 1 forms straight (air and surface) isenthalpic lines of slope $-\gamma$ emanating
 96 from the saturation vapor pressure curve, $e^*(T)$, in the state diagram of Fig. 1, provided the slight
 97 dependence of L_v on T is neglected under typical environmental conditions.



99 Figure 1. Saturation vapor pressure (e^*) curve, air (blue) and surface (green) isenthalps (Szilagyi, 2021; Crago &
 100 Qualls, 2021) during a full drying-out of the environment from completely wet to a completely dry state. The
 101 vertical and horizontal projections of the dotted lines are proportional (\propto) to the different latent ($E \leq E_w \leq E_p \leq E_p^{dry}$)
 102 and corresponding sensible (the latter negative –directed toward to surface– for E_p and E_p^{dry}) heat fluxes. See Table
 103 1 for definition of the different variables.

104 The saturation vapor pressure (hPa) can be obtained, e.g., by the Teten's formula as $e^*(T) =$
 105 $6.108\exp[17.27T / (237.3 + T)]$ where T is supplied in $^{\circ}\text{C}$ (Stull, 2000). The wet-bulb
 106 temperature, T_{wb} , is the lowest temperature the air at the measurement height can attain by
 107 evaporation, but this temperature is rarely reached during natural processes due to large-scale
 108 vertical mixing of free tropospheric air into the boundary layer (Brutsaert, 1982). Instead, a wet
 109 environment air temperature, $T_{PT} \geq T_{wb}$, generally occurs. T_{PT} however is not known during
 110 drying conditions of the environment (i.e., when $T_a > T_{PT}$), but it can be estimated by the wet-
 111 surface temperature, T_{ws} , because in humid conditions air temperature changes mildly with
 112 elevation above the ground (Laikhtman, 1964; Stull, 2000; Szilagyi, 2014).

113 T_{ws} can be estimated (Szilagyi & Jozsa, 2008) by writing out the Bowen ratio (i.e., H / LE) for a
 114 small wet patch utilizing the Penman (1948) equation for E_p (mm d^{-1}), yielding the evaporation
 115 rate of such a small wet area, as

$$116 \quad \frac{H}{LE} = \frac{Q_n - E_p}{E_p} \approx \gamma \frac{T_{ws} - T_a}{e^*(T_{ws}) - e_a} \quad (2)$$

117 where the small size of the wet patch means it cannot alter the temperature and humidity of the
 118 overpassing air significantly, measured upwind of it. Note that E specified in water depth can be
 119 transformed into energy flux (LE) values by $LE = L_v \rho_w E$, and vice-versa for Q_n , where ρ_w is the
 120 density of water. Eq. 2 is implicit for T_{ws} , requiring iterations to solve. The Penman equation is
 121 given by

$$122 \quad E_p = \frac{\Delta Q_n}{\Delta + \gamma} + \frac{\gamma f_u [e^*(T_a) - e_a]}{\Delta + \gamma} \quad (3)$$

123 where Δ denotes the slope of the saturation vapor pressure curve ($\text{hPa } ^{\circ}\text{C}^{-1}$) at the measured air
 124 temperature T_a , and the empirical wind function, f_u ($\text{mm d}^{-1} \text{ hPa}^{-1}$), is traditionally specified as f_u
 125 $= 0.26(1 + 0.54u_2)$ (Brutsaert, 1982). Here u_2 (m s^{-1}) is the horizontal wind speed at 2-m above
 126 the ground and can be estimated by a power function (Brutsaert, 1982) from measurements (u_h)
 127 at h meters above the surface as $u_2 = u_h (2 / h)^{1/7}$. The $e^*(T_a) - e_a$ expression in the aerodynamic
 128 term of Eq. 3 is often referred to as the vapor pressure deficit (VPD).

129 With the two isenthalps anchored to the saturation vapor pressure curve, one may notice that
 130 during a full wet-to-dry transition of the environment the (T_a, e_a) state-coordinate points traverse
 131 the $(T_{PT} - T_a^{dry}, e_{PT} - 0)$, while the corresponding state-coordinates (T_s, e_s) track the full length of
 132 the $(T_{ws} - T_s^{dry}, e_{ws}^* - 0)$ distance on the surface isenthalp. From the two different distances
 133 travelled during the same amount of time, two different average speed values result for the
 134 movement of the respective state coordinates. By assuming that the ratio of distances travelled
 135 on the two isenthalps during any time interval equals the constant ratio of the two average speed
 136 values, a geometric similarity emerges (Szilagyi, 2021; c.f. Crago & Qualls, 2021, who used
 137 somewhat different reasoning), namely

$$138 \quad \frac{e_a}{e_{PT}} = \frac{e_s}{e_{ws}^*} \quad (4)$$

139 which can be augmented into

140
$$\frac{e_a}{e_{PT}} = \frac{e_{ws}^* - (e_{ws}^* - e_a)}{e_{ws}^* - (e_{ws}^* - e_{PT})} = \frac{e_s}{e_{ws}^*} \quad (5)$$

141 The right-hand-side of Eq. 4 can be further expanded into

142
$$\frac{e_s}{e_{ws}^*} = \frac{e_s(1 - \frac{e_a}{e_s})}{e_{ws}^*(1 - \frac{e_a}{e_s})} = \frac{e_s(1 - \frac{e_{PT}}{e_{ws}^*})}{e_{ws}^*(1 - \frac{e_{PT}}{e_{ws}^*})} = \frac{e_s - \frac{e_s}{e_{ws}^*} e_{PT}}{e_{ws}^* - e_{PT}} = \frac{e_s - e_a}{e_{ws}^* - e_{PT}} \quad (6)$$

143 The combination of Eqs. 5 and 6 yields (Szilagyi, 2021)

144
$$\frac{e_s - e_a}{e_{ws}^* - e_{PT}} = \frac{e_{ws}^* - (e_{ws}^* - e_a)}{e_{ws}^* - (e_{ws}^* - e_{PT})} \quad (7)$$

145 which via the corresponding evaporation terms in Fig. 1 can be written as

146
$$\frac{E}{E_w} = \frac{E_p^{dry} - E_p}{E_p^{dry} - E_w} \quad (8)$$

147 due to the Dalton-type formulation of any evaporation term as $E = -K de/dz = K_z(e_s - e_a)$ where
 148 K is the turbulent diffusion coefficient, z is vertical distance and K_z is K divided by the
 149 measurement height.

150 In Eq. 8, E_p^{dry} can be obtained by Eq. 3 with the $e_a = 0$ substitution, and e^* and Δ evaluated at the
 151 dry-environment air temperature, $T_{dry} (= T_a + e_a / \gamma)$ (Szilagyi, 2021). The wet-environment
 152 evaporation rate, E_w , can be obtained from the Priestley-Taylor (1972) equation as

153
$$E_w = \alpha \frac{\Delta(T_{PT})Q_n}{\Delta(T_{PT}) + \gamma} \quad (9)$$

154 The unknown wet-environment air temperature, T_{PT} , can be substituted by the lesser of T_{ws} and
 155 T_a because T_{PT} can never exceed T_a due to the cooling effect of evaporation, while T_{ws} can during
 156 high relative-humidity conditions (Szilagyi, 2014, 2021). The spatially and temporally constant
 157 value of the Priestley-Taylor (PT) coefficient, α , can be set without any calibration with gridded
 158 data, covering a large spatial domain and thus ensuring the presence of permanently or
 159 periodically wet areas, by the method of Szilagyi *et al.* (2017), otherwise, it must be calibrated,
 160 typically within the [1 – 1.32] interval (Morton, 1983).

161 Eq. 8 can be rearranged after dividing it by E_p (Szilagyi *et al.*, 2017; Crago & Qualls, 2018) into

162
$$y = X; \quad y := \frac{E}{E_p}, \quad X := w_i \frac{E_w}{E_p}, \quad w_i := \frac{E_p^{dry} - E_p}{E_p^{dry} - E_w} \quad (10)$$

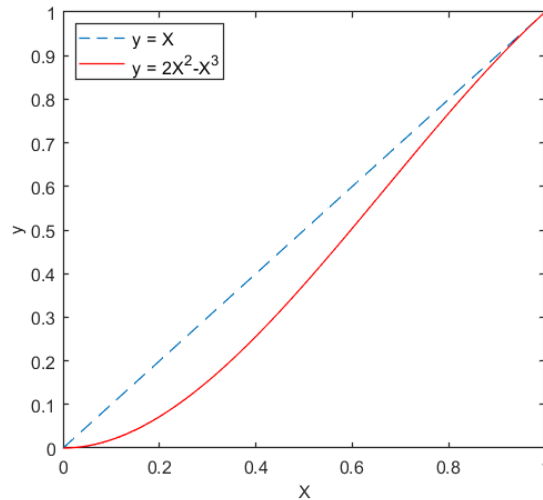
163 which is a linear relationship between the two nondimensional variables y and X . Notice that w_i
 164 acts as a wetness index, with $w_i \approx 0$ for hyper arid and $w_i = 1$ for wet conditions (Szilagyi *et al.*,
 165 2017). Note also that the two nondimensional variables were already obtained by Szilagyi *et al.*
 166 (2017) in a different way, before the present thermodynamic-based derivation was found. The
 167 complementarity in the CR means that E and E_p change in opposite ways (Bouchet, 1963), best
 168 seen in Eq. 10 between E and $E_p X$. When E_p increases (i.e., the environment dries), w_i decreases
 169 while E_w remains unchanged, yielding a decreased E rate.

170 As an area dries, large-scale horizontal advection of more humid air from the surrounding larger
 171 region may occur. This is especially true for areas lying downwind from a sea, or other large
 172 body of water, or areas surrounded by mountains having much wetter conditions. This influx of
 173 external humid air suppresses or completely eliminates the weak vertical humidity gradient that
 174 would otherwise exist. This means that the resulting suppressed and therefore vanishing $e_s - e_a$
 175 term in Eq. 7 would not respond anymore to changes in e_s and therefore to the ensuing e_a that a
 176 change in e_s would normally generate, leaving the left-hand-side of Eq. 7 unresponsive to any
 177 changes in (the transported) e_a itself, thus causing $dy / dX \rightarrow 0$ when $X \rightarrow 0$ (Szilagyi, 2021).
 178 Note that e_{ws}^* and e_{PT} are conservative (invariant) quantities only under isenthalpic processes and
 179 any humidity advection violates this adiabatic requirement but the resulting changes in e_{ws}^* and
 180 e_{PT} are treated negligible in this study (as in Szilagyi, 2021) which is probably acceptable as long
 181 as the humidity transport itself is not too excessive.

182 With consideration of the four boundary conditions (BC) of i) $y = 1 | X = 1$; ii) $dy / dX = 1 | X=1$,
 183 iii) $y = 0 | X = 0$; iv) $dy / dX = 0 | X = 0$ and seeking a polynomial solution, the following
 184 nondimensional complementary relationship

$$185 \quad y = 2X^2 - X^3 \quad (11)$$

186 is obtained (Szilagyi et al., 2017; Szilagyi, 2021). Note also that when the horizontal advection of
 187 humidity is negligible then the last BC is absent, yielding the linear form, Eq. 10, of the CR.
 188 Figure 2 depicts the two solutions.



190 Figure 2. The linear and nonlinear polynomial CR relationships between $y = E E_p^{-1}$ and $X = w_i E_w E_p^{-1}$.

191 Eq. 11 has already been applied on a monthly basis in a calibration-free mode, employing a
 192 spatially and temporally constant PT- α value with great success (outperforming mainstream
 193 complex, data-intensive evaporation models) over the US (Szilagyi et al., 2017; Kim et al., 2019;
 194 Ma & Szilagyi, 2019; Ma et al., 2020), China (Ma et al., 2019), and the globe (Ma et al., 2021).
 195 It is distinct from a similar model formulation of Liu et al. (2018), and Brutsaert et al. (2020) in
 196 two important aspects. Firstly, in the evaluation of Δ within the PT-equation the latter sources

197 ignore the temperature change between actual (i.e., drying) and wet environmental conditions.
 198 Secondly, and more importantly, in their nondimensional variable, x , playing the role of X here,
 199 the wetness index, w_i , does not appear as their derivation of x is heuristic, not based on
 200 thermodynamics. As a result, their $x = E_w E_p^{-1}$ value can only approach zero when the available
 201 energy at the surface, Q_n , does so in E_w , since E_p is bounded. In order to broaden the resulting
 202 limited range of the x values the PT- α value must be lowered significantly with growing aridity,
 203 much below its physically meaningful lower-bound value of unity. Their treatment of the PT- α
 204 simply as a tunable parameter thus negates the original purpose of the PT-equation, which is to
 205 account for the entrainment of free tropospheric air into the boundary layer (Lhomme, 1997)
 206 strictly under wet environmental conditions. See Szilagyi et al. (2020) for an in-depth discussion
 207 of this issue.

208 Table 1. List of the different evaporation (E) rates employed in the study together with the relevant temperature (T)
 209 and vapor pressure (e) terms defined.

E, LE	Actual evaporation, latent-heat rate
E_p	Potential (Penman) evaporation rate
E_p^{dry}	Dry-environment potential evaporation rate
E_w	Wet-environment (Priestley-Taylor) evaporation rate
$T_a, e_a [= e^*(T_d)]$	Actual air temperature, vapor pressure
T_a^{dry}	Dry-environment air temperature
T_d	Dew-point temperature
T_{PT}, e_{PT}	Wet-environment air temperature, vapor pressure
T_{wb}, e_{wb}^*	Wet-bulb temperature, vapor pressure
T_s, e_s	Actual land-surface temperature, vapor pressure
T_s^{dry}	Dry-environment land surface temperature
T_{ws}, e_{ws}^*	Wet surface temperature (Szilagyi and Jozsa, 2008), vapor pressure

210

211 3. Expansion of the polynomial complementary relationship by a power function approach

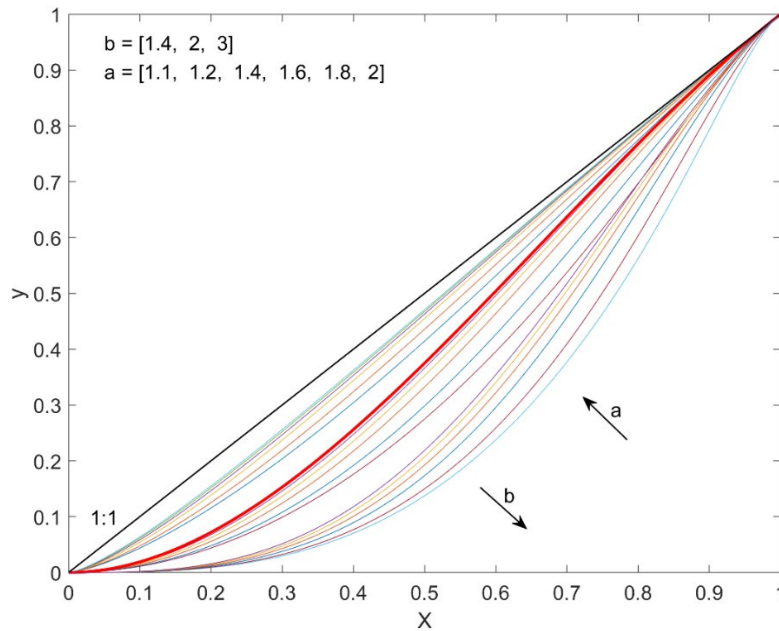
212 The polynomial in Eq. 11 can be expanded by a power-function approach using the same BCs.
 213 The resulting function

$$214 \quad y = aX^b - (a - 1)X^{\frac{ab-1}{a-1}} \quad a, b > 1 \quad (12)$$

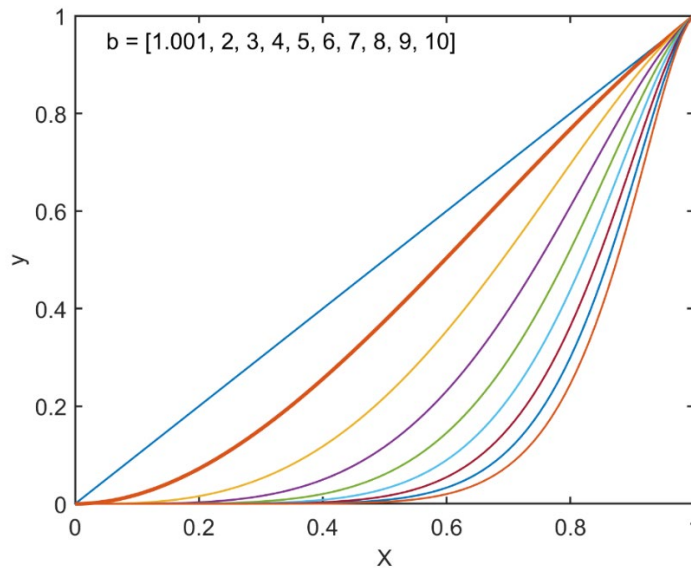
215 has two parameters additional to Eq. 11, a and b . Fig. 3 displays the ensuing curves for selected
 216 values of a and b . With the value of b increasing (from 1.4 to 2 to 3) the curves move to the
 217 right, forming three groups of curves with the a and b values picked for demonstration. Within
 218 each group the curves move upward with increasing values of a . For example, the lowest (i.e.,
 219 right-most) curve has $a = 1.1$ and $b = 3$, while the one just above it belongs to $a = 1.2, b = 3$. For
 220 most practical applications the parameter ranges can be narrowed to $1 < a \leq 2$ and $1 < b < 10$.

221 In order to reduce the number of parameters to just two (the PT- α , and b) in Eq. 12 for a
 222 meaningful comparison with other existing two-parameter CR-based methods, $a = 2$ is
 223 prescribed in this study for evaporation estimation. It makes also possible that the power-
 224 function curve revert to the polynomial of Eq. 11 during calibration when necessary. Fig. 4

225 displays the curves with a prescribed value $a = 2$, and $1 < b \leq 10$. The curve with $a = 2$ and $b =$
 226 1.001 indeed has a vanishing slope at $X = 0$, as BC iv) requires, but it is indistinguishable from
 227 the $y = X$ line of Eq. 10 by the naked eye. For this reason, during calibration of b in the ensuing
 228 analysis with $a = 2$ imposed, a value of $b = 1$ will be allowed for practicality, even though it
 229 violates BC iv).



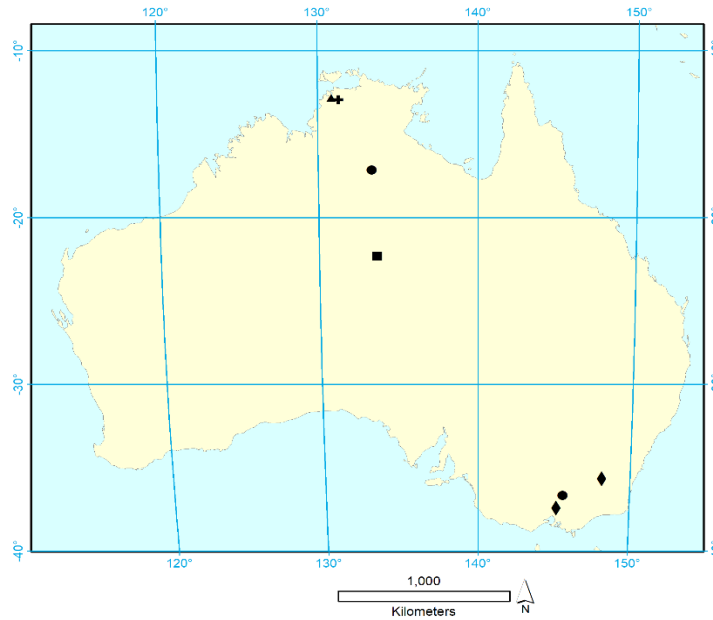
231 Figure 3. Graphical representation of Eq. 12 for selected values of a and b . The polynomial of Eq. 11 ($a = b = 2$) is
 232 the heavier red line.



234 Figure 4. Graphical representation of Eq. 12 for $a = 2$ and $1 < b \leq 10$. The polynomial of Eq. 11 ($a = b = 2$) is the
 235 heavier red line.

236 **4. Testing the power-function approach with eddy-covariance data**

237 The polynomial (Eq. 11) as well as the power-function (Eq. 12) formulations of the CR are tested
238 with eddy-covariance data of seven Australian FLUXNET sites, displayed in Fig. 5. These sites
239 include land covers of grass, permanent wetland, open shrubland, woody savanna, and evergreen
240 broadleaf forests. See Table 1 in *Crago & Qualls (2018)* for more information on the
241 measurements, and Table 4 below for geographic coordinates and periods of record. In the
242 ensuing modeling measurement heights for wind speed are reduced by the average height of the
243 vegetation. The daily eddy-covariance-measured LE fluxes are Bowen-ratio corrected [i.e., $LE_c =$
244 $Q_n (1+H LE^{-1})$] to close the energy budget (*Twine et al., 2000*), and the temperature values
245 converted to potential temperatures, $T_p = T_a + gz_m / c_p$, where z_m is the measurement height for air
246 temperature, and g is the gravitational acceleration (e.g., *Stull, 2000*) due to the relatively large
247 scatter in z_m among the sites (from 2.5 m for grass to 70 m for the forests). Note that in theory, T_p
248 must replace T_a in the preceding equations (as sensible heat fluxes are driven by vertical
249 gradients of T_p and not T_a), but the difference between them is negligible for measurement
250 heights not far from the ground in comparison to the observed vertical change in T_a .



252 Figure 5. Location of the seven FLUXNET sites (see Table 4 for exact coordinates) with at least one year of daily
253 meteorological and eddy-covariance derived flux measurements. ✚: permanent wetland; ▲: woody savanna; ■: open
254 shrubland; ●: grassland; ◆: evergreen broadleaf forest.

255

256 The evaporation estimates of Eqs. 11 and 12, employing daily, 5- and 30-day aggregated input
257 data are compared to similar estimates of three additional two-parameter heuristic CR-based
258 models by *Kahler & Brutsaert (2006)*, *Han & Tian (2012)*, and *Gao & Xu (2021)*, to be referred
259 to as KB06, HT12 and GX21, respectively. In all three models and in Eq. 12, the two tunable
260 parameters include the $PT-\alpha$ and an additional parameter (Table 2) for a meaningful comparison

261 of the CR models. The exact representation of HT12 is chosen specifically for such a purpose of
 262 a shared PT- α .

263 Table 2 summarizes the three models. KB06 and HT12 evaluate Eq. 9 at the drying air
 264 temperature, T_a , while GX21 adopts the approach of *Szilagyi & Jozsa (2008)* for estimating T_{ws}
 265 and thus T_{PT} (*Szilagyi, 2014*). For additional information of the models, please, refer to the
 266 relevant publication.

267
 268 Table 2. Summary of the three additional two-parameter CR-based models employed in this study.

KB06	HT12*	GX21
$y = (1 + c^{-1})x - c^{-1}$ $x_{KB} = E_w(T_a) E_p^{-1}$	$y = [1 + k(x^{-1} - 1)^n]^{-1}$ $x_{HT} = \alpha^{-1} E_w(T_a) E_p^{-1}$ $x_h = (0.5 + c_{HT}^{-1})[\alpha(1 + c_{HT}^{-1})]^{-1}$ $n = 4\alpha(1 + c_{HT}^{-1})x_h(1 - x_h)$ $k = [x_h(1 - x_h)^{-1}]^n$	$y = \exp[(1 - x^{-d})d^{-1}]$ $x = E_w E_p^{-1}$
Parameters: α, c	Parameters: α, c_{HT}	Parameters: α, d

269 *Written in the form specified in *Han & Tian (2018)*.

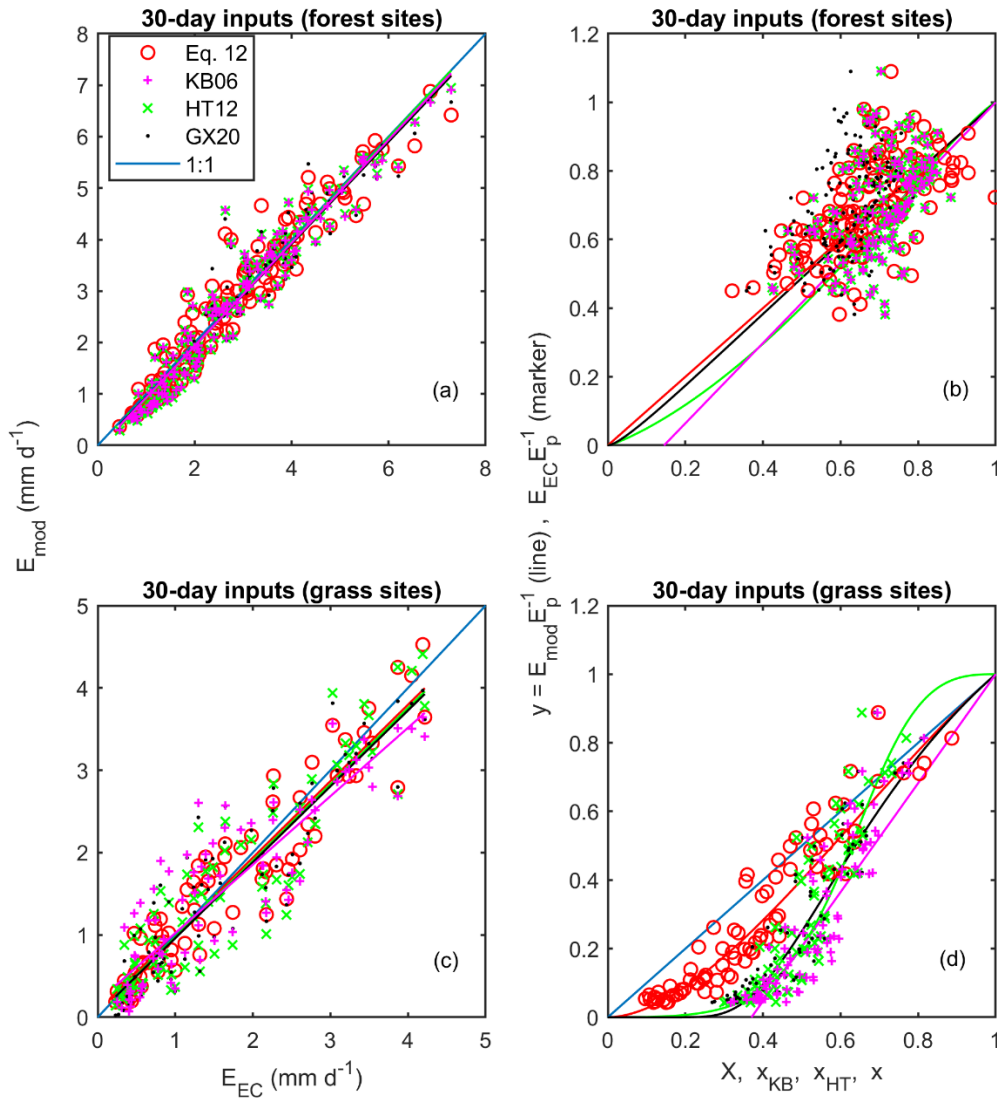
270

271 A 5-day aggregation instead of a weekly one is chosen, because *Morton (1983)* argues that it is
 272 the shortest time-interval over which any effect of passing weather systems, temporarily
 273 upsetting the dynamic equilibrium between the surface and the overlying air, can be expected to
 274 be substantially subdued.

275 Performance of the calibrated models is summarized in Table 3. The four (plus Eq. 11) models
 276 behave similarly in terms of the root-mean-square error (RMSE), but Eq. 12 produces the best
 277 results in seven out of the nine cases considered, followed by Eq. 11 (four occasions, provided
 278 Eq. 12 is excluded) and KB06 (twice). In fact, Eq. 12 is always the best performing model with
 279 30-day aggregated data. In KB06 the calibrated values of the PT- α occasionally drop below the
 280 physically meaningful unity value while it is almost the norm for GX21. Interestingly, the best-
 281 fit-line slope deviates from its optimal value of unity the least with Eq. 11.

282 Fig. 6 demonstrates the increasing effect of large-scale horizontal moisture transport on the shape
 283 of the nondimensional CR curve of Eq. 12, as aridity progresses. For the evergreen broadleaved
 284 forests serious aridity never occurs as the majority of the points are situated at $X > 0.5$ (Fig. 6b),
 285 with corresponding evaporation rates, $E_{EC} > 1 \text{ mm d}^{-1}$ (Fig. 6a), therefore the effect of any
 286 possible horizontal moisture transport toward these sites remains negligible. As a result,
 287 calibration of Eq. 12 yields $b \rightarrow 1$ and thus the straight line of Eq. 10 (red line in Fig. 6b, on top
 288 of the 1:1 line). More serious aridity, on the other hand, can develop over the grass sites resulting
 289 in several points at $X < 0.2$ (Fig. 6d), and $E_{EC} < 0.5 \text{ mm d}^{-1}$ (Fig. 6c). Any horizontal moisture
 290 transport to the grass sites somewhat drier than their environs will leave the eddy-covariance
 291 measurements largely unaffected in the beginning of drying when vertical gradients of the vapor
 292 pressure over the grass are still significant, but nonetheless, will depress the value of E_p (which is

293 very sensitive to moisture changes in its VPD term due to the steep slope of the saturation vapor
 294 pressure curve at high temperatures), and thus boost the wetness index, w_i , within X , which then
 295 moves the measurement points to the right horizontally in Fig. 6d, away from the 1:1 line for 0.2
 296 $< X < 0.45$. The measurement points however will follow the diminishing slope of Eq. 12 at
 297 extreme low $X (< 0.2)$ values (as seen in Fig. 6d) and get closer to the 1:1 line again when large-
 298 scale horizontal moisture advection itself weakens as arid conditions probably spread spatially.



300 Figure 6. Regression plots of the modeled (E_{mod}) 30-day evaporation rates against eddy-covariance measurements
 301 (E_{EC}) at two forested (a) and two grass (c) sites of FLUXNET in Australia (see Fig. 5 for locations) together with the
 302 least-squares-fitted straight lines. Graphical representation of the calibrated (see Table 3) nondimensional formulas
 303 (b, d) listed in Table 2 plus that of Eq. 12, displayed with the nondimensional E_{EC} measurements. Color coding for
 304 the best-fit lines and the theoretical curves comes from the markers.

305 Note that the 1:1 line forms a theoretical upper limit to the measured nondimensional
 306 evaporation rates for KB06 and GX21 only, as these models relate $E E_p^{-1}$ to $E_w E_p^{-1}$ with the $E \leq$
 307 E_w expectation. While such is the case mostly for the grass sites (Fig. 6d), it is not so for the
 308 forested ones (Fig. 6b), due to their incorrect scaling that produces x_{KB} and x (Table 2),
 309 respectively, instead of the thermodynamically backed one for X , first suggested by Szilagyi et
 310 al. (2017).

311 Table 3. Root-mean-square error (RMSE) values (in mm d⁻¹ for easier comparison among aggregation periods) of
 312 the CR-based two-, and single-parameter (Eq. 11) evaporation estimation methods at different Australian
 313 FLUXNET sites displayed in Fig. 5. The trial-and-error-calibrated parameter values of the different methods are also
 314 displayed, together with the resulting slope (m) of the best-fit line. The lowest RMSE values among the two-
 315 parameter methods are displayed in bold for each aggregation period and group of sites considered. The single-
 316 parameter estimate (Eq. 11) is bold-faced when it yields better estimates than the two-parameter methods (without
 317 Eq. 12).

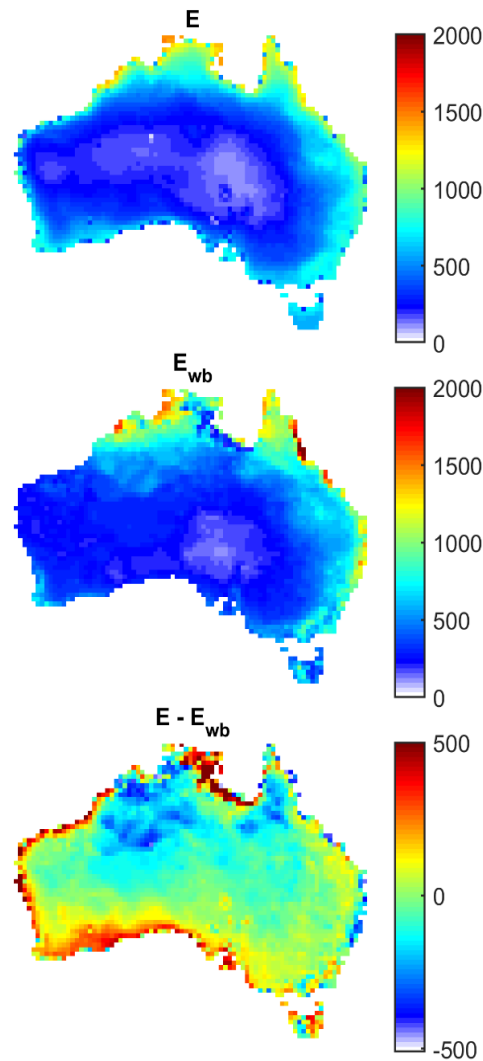
Station/aggregation	Eq. 12	Eq. 11	KB06	HT12	GX21
All (seven sites)	0.81	0.89	0.84	0.84	0.86
Daily	$\alpha=1.11, b=1.3$ $m=0.83$	$\alpha=1.16$ $m=0.94$	$\alpha=1.04, c=1.95$ $m=0.84$	$\alpha=1.09, c_{HT}=1.3$ $m=0.86$	$\alpha=0.93, d=1.07$ $m=0.85$
5-day	0.66	0.72	0.71	0.7	0.71
	$\alpha=1.13, b=1.45$ $m=0.87$	$\alpha=1.17$ $m=0.96$	$\alpha=1.08, c=1.6$ $m=0.9$	$\alpha=1.13, c_{HT}=1.1$ $m=0.91$	$\alpha=0.97, d=1.35$ $m=0.9$
30-day	0.51	0.56	0.58	0.59	0.59
	$\alpha=1.14, b=1.55$ $m=0.91$	$\alpha=1.17$ $m=1$	$\alpha=1.1, c=1.5$ $m=0.95$	$\alpha=1.14, c_{HT}=1.1$ $m=0.94$	$\alpha=0.98, d=1.38$ $m=0.93$
Grass (two sites)	0.7	0.72	0.83	.75	0.75
Daily	$\alpha=1.12, b=1.65$ $m=0.75$	$\alpha=1.18$ $m=0.83$	$\alpha=0.96, c=2.25$ $m=0.66$	$\alpha=1.15, c_{HT}=0.9$ $m=0.75$	$\alpha=0.96, d=1.46$ $m=0.74$
5-day	0.55	0.57	0.69	0.61	0.6
	$\alpha=1.16, b=1.75$ $m=0.83$	$\alpha=1.21$ $m=0.9$	$\alpha=1.02, c=1.85$ $m=0.75$	$\alpha=1.18, c_{HT}=0.9$ $m=0.81$	$\alpha=1.02, d=1.73$ $m=0.84$
30-day	0.37	0.38	0.55	0.48	0.46
	$\alpha=1.21, b=1.85$ $m=0.93$	$\alpha=1.24$ $m=0.98$	$\alpha=1.06, c=1.7$ $m=0.83$	$\alpha=1.24, c_{HT}=0.8$ $m=0.93$	$\alpha=1.05, d=1.81$ $m=0.92$
Forest (two sites)	0.75	0.92	0.65	0.67	0.7
Daily	$\alpha=1.11, b=1$ $m=0.93$	$\alpha=1.15$ $m=0.98$	$\alpha=0.94, c=46.4$ $m=0.96$	$\alpha=1, c_{HT}=5$ $m=1$	$\alpha=0.86, d=0.1$ $m=0.96$
5-day	0.55	0.66	0.52	0.53	0.55
	$\alpha=1.12, b=1$ $m=0.94$	$\alpha=1.16$ $m=1$	$\alpha=0.98, c=7.64$ $m=0.98$	$\alpha=1, c_{HT}=4.4$ $m=1$	$\alpha=0.88, d=0.1$ $m=0.98$
30-day	0.4	0.48	0.42	0.41	0.43
	$\alpha=1.13, b=1$ $m=0.98$	$\alpha=1.17$ $m=1.06$	$\alpha=1, c=5.9$ $m=1$	$\alpha=1, c_{HT}=5$ $m=1.01$	$\alpha=0.89, d=0.1$ $m=0.99$

318

319 Testing the power-function approach with gridded simplified water-balance data

320 Eq. 12 is further tested across Australia for the spatial distribution of its b value, employing 0.25-
 321 degree monthly estimates of E_w, E_p and E_p^{dry} calculated with data from sources specified in the
 322 global study of Ma et al. (2021), except that R_n now comes from the Global Land Data
 323 Assimilation System Version 2.1 (Beaudoin & Rodell, 2020). The above monthly evaporation

324 terms are aggregated to 0.5-degree spatial resolution over the 2003-2012 time period together
 325 with the 0.25-degree precipitation values from the Global Precipitation Climatology Center
 326 (GPCC) Full Data Monthly Version 2018 (Schneider *et al.*, 2018). Multi-year, simplified water-
 327 balance derived evaporation (E_{wb}) rates as precipitation less runoff are calculated on a cell-by-
 328 cell basis by taking the arithmetic mean of two monthly 0.5-degree gridded global runoff rates
 329 from the gauge-derived database of Ghiggi *et al.* (2019), and the synthesis of eleven land surface
 330 models by Hobeichi *et al.* (2019). The two sources of the runoff values are necessary due to the
 331 scarcity and uneven distribution of the monitoring watersheds (Fowler *et al.*, 2021) across
 332 Australia large enough to accommodate the model cells. As only the multi-year mean annual E_{wb}
 333 values are needed for the present purpose of investigating the spatial distribution of b in Eq. 12,
 334 any possible changes in annual cell-water storage can be assumed to exert a negligible influence
 335 on the multiyear E_{wb} value (Brutsaert, 1982) and especially on the spatial distribution
 336 characteristics of b .



338 Figure 7. Spatial distribution of the 0.5-degree multiyear (2003-2012) mean annual evaporation rates (mm a⁻¹) across
 339 Australia by a) Eq. 11; b) simplified water balance (E_{wb}), and; c) their difference.

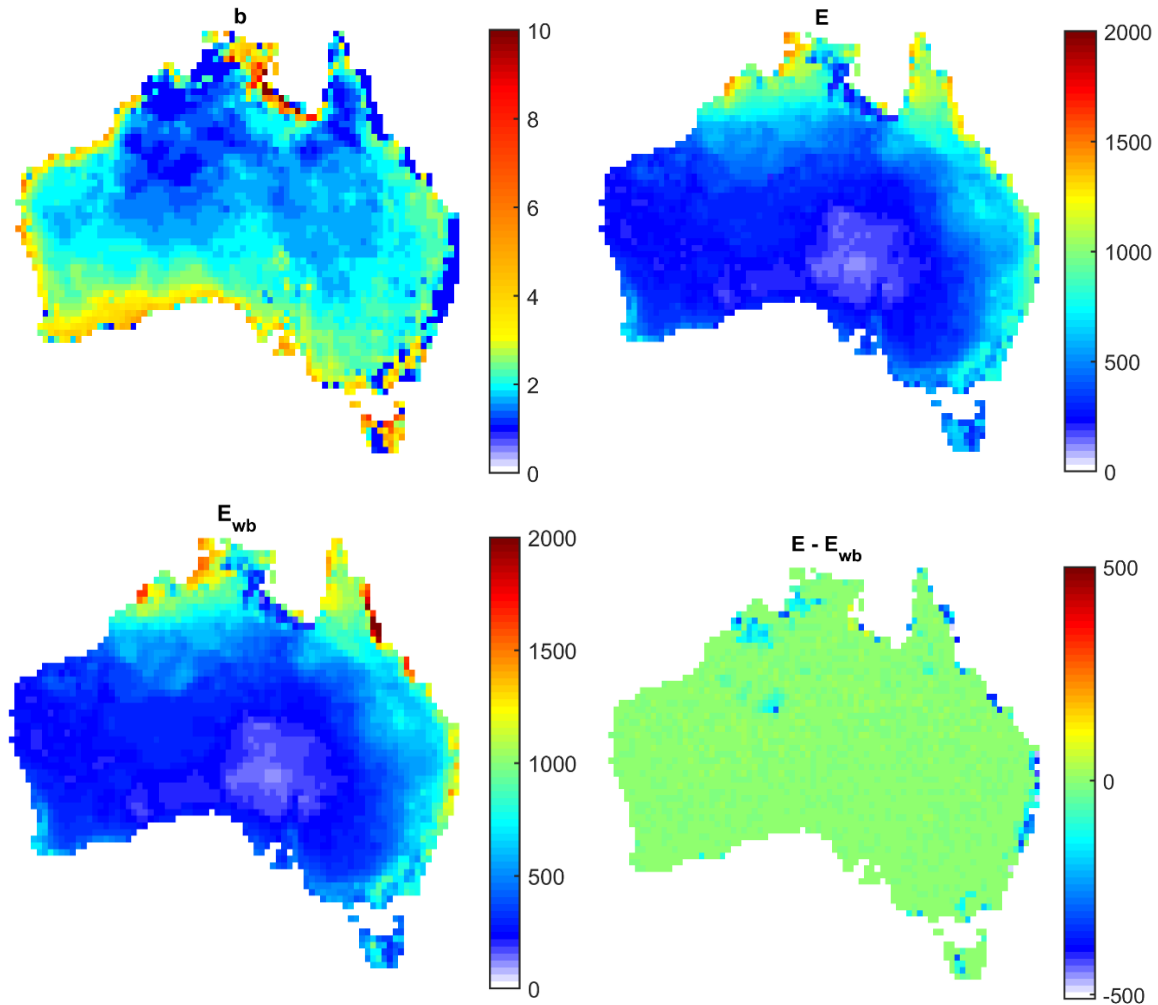
340 The polynomial equation (Eq. 11) without any calibration, estimates (Fig. 7) the continent-wide
341 (with Tasmania included) multiyear mean annual water-balance evaporation (E_{wb}) rate of 462
342 mm a⁻¹ within 4% ($E = 447$ mm a⁻¹). The value of the PT- α in Eq. 11 was set to 1.1 globally by
343 *Ma et al.* (2021) via the method of *Szilagyi et al.* (2017), requiring no calibration, therefore no
344 precipitation or runoff data. (Note that such a calibration-free setting of the PT- α value can only
345 be performed for large-scale data sets ensuring the presence of permanently or at least
346 periodically wet areas within their spatial domain.)

347 The polynomial CR (Eq. 11) overestimates the water-balance evaporation rates near the southern
348 and western seashore where the prevailing winds carry moisture laden air from the ocean to the
349 land, thus decoupling its moisture content from that of the underlying arid or semi-arid land
350 surface. Naturally, the more arid the land is, the stronger this overestimation. The strongest
351 overestimation, however, occurs along the western side of the Gulf of Carpentaria in the north
352 where the E_{wb} values are unusually low along a south-west to north-east patch, for reasons not
353 known to these authors. Otherwise, Eq. 11 generally underestimates the water-balance values in
354 northern Australia characterized by a monsoonal precipitation regime, for reasons discussed
355 below.

356 The value of the parameter b in Eq. 12 ($a = 2$, $\alpha = 1.1$) is calibrated on a cell-by-cell basis by
357 minimizing the absolute difference in the multi-year mean annual model-estimated and water-
358 balance derived evaporation rates. Fig. 8a displays the resulting spatial distribution of the
359 calibrated values. As seen, the spatial pattern of the values strongly follows that of the estimation
360 error in Fig. 7: elevated values where the estimation error is positive and depressed ones where it
361 is negative. This is to be expected, as the measurement points (E_{wb} or E_{EC}) are fixed in the
362 nondimensional graph once the value of α is set within X . An overestimation (i.e., when the
363 curve is above a given marker point in e.g., Fig. 6d) in Eq. 12 can only be corrected by moving
364 the curve to the right which is achieved by increasing the value of b (Fig. 4), and vice versa for
365 an underestimation.

366 Naturally, the calibration yields model estimates very close to the ‘observed’ values (Fig. 8b, c,
367 d) in each cell with only a low number of exceptions. The multiyear mean annual value though
368 remains practically the same ($E = 448$ mm a⁻¹) as before, suggesting that the $b = 2$ value implicit
369 in Eq. 11 and therefore Eq. 11 itself with its rational boundary conditions, is physically well
370 founded and indeed obeyed by nature, at least, in a statistical sense. The histogram of the
371 calibrated values of b (Fig. 9) with an ensemble mean of 2.08 and a median value of 1.9, further
372 corroborates this finding.

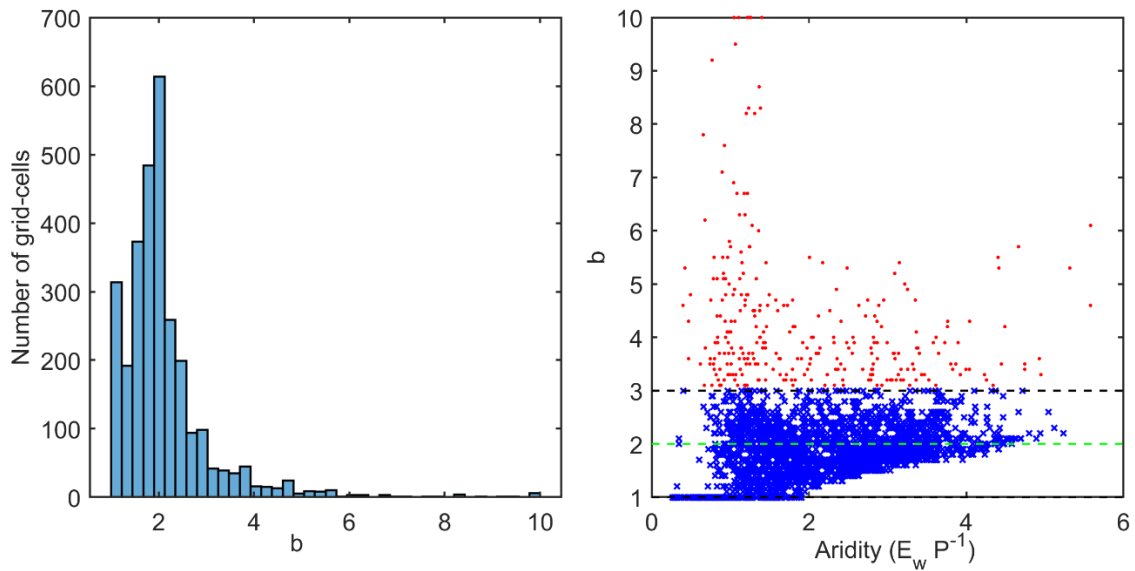
373



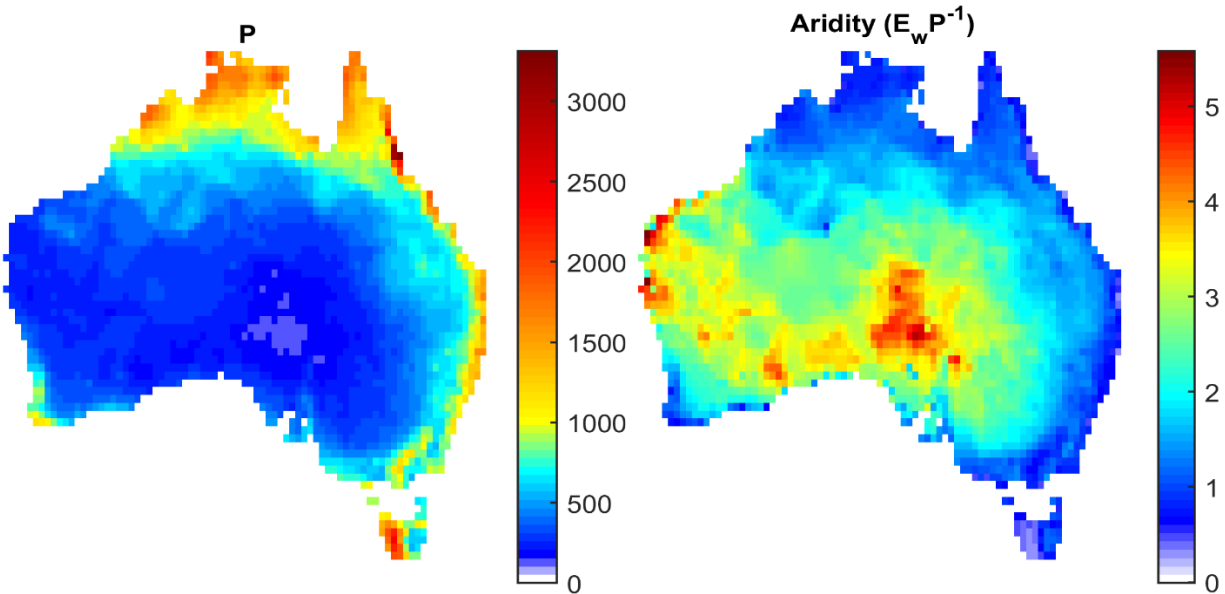
376 Figure 8. Spatial distribution of the a) calibrated value of b in Eq. 12; b) resulting multi-year (2003-2012) mean
 377 annual evaporation rates (mm a^{-1}) by Eq. 12 (E); c) simplified water-balance (E_{wb}) estimates for comparison, and;
 378 their difference.

379 An interesting property of the histogram is that it is bimodal, with a secondary peak near $b = 1$.
 380 As discussed above, a unity value of b and a linear relationship between y and X (except in the
 381 vicinity of $X = 0$ where the slope must vanish due to the BCs in Eqs. 11 and 12) result in theory
 382 when in Fig. 1 the relative speed of the state coordinates along the isenthalps stays constant
 383 during drying out of the environment (until hyper arid conditions are reached near $X = 0$). Such
 384 conditions however may most commonly exist while the environment remains relatively humid
 385 as seen at the forest sites, and thus, the effect of any possible large-scale horizontal moisture
 386 transport toward the drying area continues to be negligible. Indeed, this must be the case along
 387 almost the entire eastern coast of Australia, the north-western part of the Northern Territory, the
 388 eastern side of the Gulf of Carpentaria, within the Australian Alps as well as the western part of
 389 Tasmania, all where annual precipitation rates are the highest and aridity the lowest (Fig. 10),
 390 forcing the calibrated values of b to remain unity (Fig. 8a).

391



394 Figure 9. a) Histogram of the b values obtained via a cell-by-cell calibration of Eq. 12 against the multiyear mean
 395 annual E_{wb} rate. b) The calibrated b values plotted against the aridity index (ratio of the wet-environment
 396 evaporation rate, E_w , and precipitation), marked by red dots when $b > 3$.



398 Figure 10. Spatial distribution of the multi-year (2003-2012) mean annual precipitation (P) rates (mm a^{-1}) and the
 399 aridity index (ratio of the wet-environment evaporation rate, E_w , and P).

400 As seen in Fig. 9, about 95% of the histogram values are less than three. In fact, $b > 3$ occurs
 401 predominantly along the dry southern and western seashore (Fig. 8a) as a result of an
 402 overestimation of Eq. 11 (Fig. 7) due to the significant moisture transport from the ocean
 403 decoupling the moisture status of the air from its land surface. (A similar overestimation by Eq.
 404 11 along the western side of the Gulf of Carpentaria is most likely the consequence of the
 405 underestimated water-balance-derived values in Fig. 8c). The calibrated $b < 3$ values, assumed to

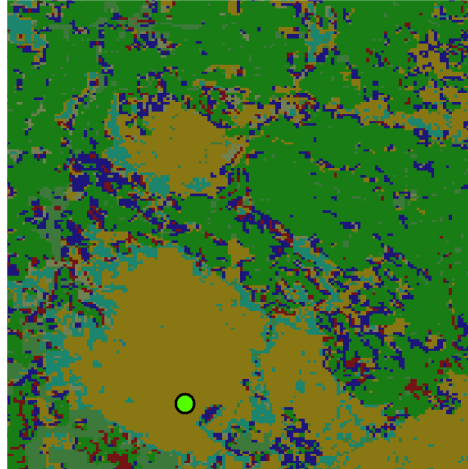
406 represent the required coupled state (with only minimal advection) of the air and the underlying
 407 land surface, scatter around the value of two in Fig. 9b but with a decreasing range and an
 408 increasing lower envelope as aridity grows. When the aridity index is less than about unity,
 409 signifying wet environmental conditions, the predominant value of b becomes unity, as discussed
 410 above. The scatter in the b values of Fig. 9b makes it hard to predict the value of b based on
 411 some index of environmental aridity, except when the environment is either very humid ($b \rightarrow 1$)
 412 or increasingly arid ($b \rightarrow 2$). This is not surprising, as the value of b generally depends on the
 413 strength of the horizontal moisture advection which in turn is influenced by the existing moisture
 414 difference between the study area and its larger, regional environment. This dynamic interplay
 415 explains the underestimation of Eq. 11 in the monsoonal northern part of Australia, where in the
 416 wet phase of the monsoon the $b = 2$ value implicit in Eq. 11 (instead of the calibrated b values
 417 close to unity seen in Fig. 8a) underestimates the wet evaporation rates while in the dry phase of
 418 the monsoon with its lower land evaporation rates it cannot make up for it, even when the $b = 2$
 419 value then is probably correct.

420 The consistency in the spatial distribution of the calibrated b values is perhaps most striking
 421 when one compares the gridded-data-derived values with those obtained from the FLUXNET
 422 measurements, both listed in Table 4. Only at the southernmost site is there a significant
 423 difference in the two calibrated values, where the large-scale horizontal moisture transport from
 424 the nearby (about 70 km away) ocean is felt by the grid cell covering not only the forest but other
 425 land-covers (*ESA*, 2009) expected to be drier than the forested land (Fig. 11).

426 Table 4. Calibrated values of b in Eq. 12 from the FLUXNET 30-day aggregated measurements and the monthly
 427 gridded data of *Ma et al.* (2021) for the grid-cell (2003-2012) covering the site.

FLUXNET sites in Fig. 5 (from north to south) with period of records displayed	FLUXNET site latitude, longitude (decimal degrees)	FLUXNET b	Grid-cell b
Woody savanna (2001-2014)	12.5S, 131.15E	1	1
Permanent wetland (2006-2008)	12.54S, 131.31E	1	1
Grassland (North) (2008-2014)	17.15S, 133.35E	1.7	1.6
Open shrubland (2013)	22.29S, 133.64E	2	1.9
Evergreen broadleaf forest (East) (2001-2014)	35.66S, 148.15E	1	1
Grassland (South) (2012-2014)	36.65S, 145.58E	1.9	2.3
Evergreen broadleaf forest (West) (2005-2008)	37.43S, 145.19E	1	1.9

428



430 Figure 11. Location (circle) of the evergreen broadleaf forest (West) FLUXNET site of Table 4 (last row) within the
 431 0.5-degree grid-cell covering it. The predominant land-cover category according to the United Nations Land Cover
 432 Classification System (LCCS) is ‘rainfed croplands’ in green color (ESA, 2009). The forested areas are displayed in
 433 brown. The cell is about 55 km in size.

434 Table 4 also indicates that the value of b and its spatial behavior with gridded data are not
 435 influenced or constrained by a correctly set constant value (i.e., $\alpha = 1.1$) of the PT- α since with
 436 FLUXNET data both PT- α and b are simultaneously calibrated yet yield practically the same
 437 value of b as the gridded data. A systematic increase in the correctly set constant value of the PT-
 438 α for the gridded data –in order to bring it closer to the average PT- α value of 1.14 with the 30-
 439 day aggregated FLUXNET data– results in growing differences in the two calibrated values of b
 440 at the FLUXNET sites (not shown). But this is again to be expected, as Szilagyi *et al.* (2017)
 441 pointed out that the optimal value of the PT- α is influenced by the spatial and temporal
 442 resolution of the input data itself.

443

444 5. Summary and conclusions

445 The power-function extension, Eq. 12, of the nondimensional polynomial CR of Eq. 11, the latter
 446 derived from thermodynamic considerations, introduces two parameters, a and b , additional to
 447 the PT- α in Eq. 11. By setting $a = 2$, Eq. 12 can reproduce Eq. 11 via the $b = 2$ choice, and the
 448 linear CR of Eq. 10, provided $b = 1$.

449 Calibration of the PT- α and b with FLUXNET data (while $a = 2$) results in a two-parameter CR
 450 version that excels among three additional heuristic two-parameter CR models in its estimation
 451 of the daily, 5- and 30-day aggregated latent heat fluxes. The calibrated value of b becomes unity
 452 with 30-day aggregated inputs at four FLUXNET sites, two of them situated in a wet climate
 453 with mean annual precipitation in excess of 1500 mm, while the other two sites are located in
 454 broadleaved forests enjoying about 700 mm of rain annually. At the driest, open shrubland, site
 455 the calibrated value of b becomes 2, while at the remaining two sites somewhat smaller than that.

456 With the help of gridded precipitation and runoff data the calibration of b is repeated on a cell-
 457 by-cell basis with 0.5-degree gridded monthly inputs to Eq. 12 across Australia over a whole

458 decade with a spatially and temporally constant $PT-\alpha$ value of 1.1, set by the method of *Szilagyi*
459 *et al.* (2017). The FLUXNET-derived b values are almost perfectly recaptured for the cells that
460 cover the FLUXNET sites. Only at one forest site is there a larger difference where the
461 predominant land cover of the 0.5-degree cell overlying the site is rainfed cropland which
462 probably explains the difference in the calibrated b values, i.e., unity for the forested site and 1.9
463 for the cell.

464 The grid-calibrated b values follow a bimodal distribution with a primary mode around two
465 (mean of 2.08 and median of 1.9) and a secondary one near unity. It helps explain earlier
466 findings by *Crago & Qualls* (2018) for the same FLUXNET sites, plus the current site-by-site
467 FLUXNET calibration results of why a linear nondimensional CR relationship (corresponding to
468 $a = 2, b = 1$ in Eq. 12) yields the best estimate for certain locations.

469 While *Szilagyi* (2021) in his thermodynamics-based derivation of Eq. 11 correctly deduced that a
470 vanishing slope of the corresponding curve near $X = 0$ can only occur when the difference in e_s
471 and e_a also vanishes, he failed to identify the process that can produce it in general. The spatial
472 distribution of the calibrated b values in Fig. 8, plus the site-by-site calibration results, help
473 finding it. That process is the horizontal, regional transport of humidity toward the drying area
474 which can clearly produce a vertically near constant humidity gradient and thus a vanishing
475 difference in the e_s and e_a values near $X = 0$. This horizontal humidity transport then sets the
476 second-order BC at $X = 0$ to $dy / dX = 0$ and thus produces Eq. 11. Further exploration is required
477 to explain why this polynomial solution acts as an attractor to the more flexible power-function
478 expansion (yielding a mean b value of 2.08 and a median of 1.9), considering that the polynomial
479 (just like the power-function) approach is just a mathematical convenience (satisfying the four
480 BCs) without any physically based differential equation behind it. The linear solution of Eq. 10
481 as the other attractor for the power-function curves, in contrast, results from purely
482 thermodynamic reasoning.

483 When the effect of the horizontal transport of humidity is negligible due to minimal spatial
484 differences in moisture during slight-to-moderate drying of the study region, typically in
485 permanently or at least periodically humid (due to monsoonal rains) environments, the constant
486 relative speed conjecture of the state coordinates, (e, T) vs (e_s, T_s) along the air and surface
487 isenthalps (Fig. 1), first postulated by *Szilagyi* (2021), seems to be validated by the calibrated b
488 values of unity, and thus reproducing (except near $X = 0$) the linear CR version of Eq. 10.
489 Naturally, the preservation of a constant relative speed between the two isenthalps' state
490 coordinates cannot be expected to exist in a strict sense, at all times, due to unavoidable changes
491 in Q_n , air pressure, and/or wind conditions during the averaging period (typically from day to
492 month), but rather in a statistical sense, as a mean behavior over the averaging period.

493 Eq. 12 may be preferable over the existing single-parameter (and calibration-free when applied
494 with gridded data of a large domain) polynomial approach of Eq. 11, due to its built-in flexibility
495 when calibration is made possible by available measured (e.g., eddy-covariance derived) or
496 water-balance based E estimates and/or the possibility exists that a linear CR approach (i.e.,
497 when $a = 2$ and $b = 1$ in Eq. 12) yields (even temporarily, during wet conditions that appear in
498 monsoonal regions) a better estimate than Eq. 11.

499 **Data availability** All data used in this study are publicly available from the following sites.
500 Daily FLUXNET values (<http://fluxnet.fluxdata.org/sites/site-list-and-pages/>); GPCC
501 precipitation ([https://opendata.dwd.de/climate_environment/GPCC/html/fulldata-](https://opendata.dwd.de/climate_environment/GPCC/html/fulldata-monthly_v2018_doi_download.html)
502 [monthly_v2018_doi_download.html](https://opendata.dwd.de/climate_environment/GPCC/html/fulldata-monthly_v2018_doi_download.html)); runoff data (<https://doi.org/10.6084/m9.figshare.9228176>,
503 [https://geonetwork.nci.org.au/geonetwork/srv/eng/catalog.search#/metadata/f9617_9854_8096_5](https://geonetwork.nci.org.au/geonetwork/srv/eng/catalog.search#/metadata/f9617_9854_8096_5291)
504 [291](https://geonetwork.nci.org.au/geonetwork/srv/eng/catalog.search#/metadata/f9617_9854_8096_5291)); ERA5 and ERA5-Land data ([https://www.ecmwf.int/en/forecasts/datasets/reanalysis-](https://www.ecmwf.int/en/forecasts/datasets/reanalysis-datasets/era5)
505 [datasets/era5](https://www.ecmwf.int/en/forecasts/datasets/reanalysis-datasets/era5)); R_n (https://disc.gsfc.nasa.gov/datasets/GLDAS_NOAH025_M_2.1/summary).

506

507 **Acknowledgment** Support provided by the Ministry of Innovation and Technology of Hungary
508 from the National Research, Development and Innovation Fund, financed under the TKP2021
509 funding scheme (project# BME-NVA-02), and by USDA NIFA grant IDA01584 is kindly
510 acknowledged.

511

512 **References**

- 513 Beaudoin, H., & Rodell, M. (2020). GLDAS Noah Land Surface Model L4 monthly $0.25 \times$
514 0.25 degree V2.1. Greenbelt, Maryland, USA Goddard Earth Sciences Data and Information
515 Services Center (GES DISC). <https://doi.org/10.5067/SXAVCZFAQLNO>
- 516 Bouchet, R. (1963). Evapotranspiration réelle et potentielle, signification climatique.
517 *International Association of Hydrological Sciences Publication*, 62, 134-142.
- 518 Brutsaert, W. (1982). *Evaporation into the atmosphere: Theory, history, and applications*,
519 Dordrecht. Holland: D. Reidel. <https://doi.org/10.1007/978-94-017-1497-6>
- 520 Brutsaert, W. (2015). A generalized complementary principle with physical constraints for land-
521 surface evaporation. *Water Resources Research*, 51(10), 8087-8093.
522 <https://doi.org/10.1002/2015WR017720>
- 523 Brutsaert, W., Cheng, L., & Zhang, L. (2020). Spatial distribution of global landscape
524 evaporation in the early twenty-first century by means of a generalized complementary approach.
525 *Journal of Hydrometeorology*, 21, 287-298. <https://doi.org/10.1175/JHM-D-19-480.1>
- 526 Crago, R., & Qualls, R. (2018). Evaluation of the Generalized and rescaled complementary
527 relationships. *Water Resources Research*, 54, 8086-8102.
528 <https://doi.org/10.1029/2018WR023401>
- 529 Crago R., & Qualls, R. (2021). A graphical interpretation of the rescaled complementary
530 relationship for evapotranspiration. *Water Resources Research*, 57(8).
531 <https://doi.org/10.1029/2020WR028299>
- 532 European Space Agency (ESA) (2009). GlobCover 2009. Last accessed January 15, 2022 at
533 <https://databasin.org/datasets/a08ff893bed248d2b6add102a3aa0101/>

534 Fowler, K. J. A., Acharya, S. C., Addor, N., Chou, C., & Peel, M. C. (2021). CAMELS-AUS:
535 hydrometeorological time series and landscape attributes for 222 catchments in Australia. *Earth*
536 *System Science Data*, 13, 3847-3867. <https://doi.org/10.5194/essd-570-13-3847-2021>

537 Gao, B., & Xu, X. (2020). Derivation of an exponential complementary function with physical
538 constraints for land surface evaporation estimation. *Journal of Hydrology*, 593.
539 <https://doi.org/10.1016/j.jhydrol.2020.125623>

540 Ghiggi, G., Humphrey, V., Seneviratne, S. I., & Gudmundsson, L. (2019). GRUN: an
541 observations-based global gridded runoff dataset from 1902 to 2014. *Earth System Science Data*,
542 11, 1655-1674. <https://doi.org/10.5194/essd-11-1655-2019>

543 Han, S., Hu, H., & Tian, F. (2012). A nonlinear function approach for the normalized
544 complementary relationship evaporation model. *Hydrological Processes*, 26(26), 3973-3981.
545 <https://doi.org/10.1002/hyp.8414>

546 Han, S., & Tian, F. (2018). Derivation of a sigmoid generalized complementary function for
547 evaporation with physical constraints. *Water Resources Research*, 54, 5050-5068.
548 <https://doi.org/10.1029/2017WR021755>

549 Han, S., & Tian, F. (2020). A review of the complementary principle of evaporation: From
550 original linear relationship to generalized nonlinear functions. *Hydrology and Earth System*
551 *Sciences*, 24, 2269-2285. <https://doi.org/10.5194/hess-2019-545>

552 Hobeichi, S., Abramowitz, G., Evans, J., & Beck, H. E. (2019). Linear Optimal Runoff
553 Aggregate (LORA): a global gridded synthesis runoff product. *Hydrology and Earth System*
554 *Sciences*, 23, 851-870. <https://doi.org/10.5194/hess-23-851-2019>

555 Kahler, D. M., & Brutsaert, W. (2006). Complementary relationship between daily evaporation
556 in the environment and pan evaporation. *Water Resources Research*, 42, W05413.
557 <https://doi.org/10.1029/2005WR004541>

558 Kim, D., Lee, W.-S., Kim, S. T., & Chun, J. A. (2019). Historical drought assessment over the
559 contiguous United States using the generalized complementary principle of evapotranspiration.
560 *Water Resources Research*, 55. <https://doi.org/10.1029/2019WR024991>

561 Laikhtman, D. L. (1964). *Physics of the Boundary Layer of the Atmosphere*, Sivan Press, Israel.

562 Lhomme, J. P. (1997). A theoretical basis for the Priestley-Taylor coefficient. *Boundary-Layer*
563 *Meteorology*, 82(2), 179-191. <https://doi.org/10.1023/A:1000281114105>

564 Liu, X., Liu, C., & Brutsaert, W. (2018). Investigation of a generalized nonlinear form of the
565 complementary principle for evaporation estimation. *Journal of Geophysical Research:*
566 *Atmospheres*, 123(8), 3933-3942. <https://doi.org/10.1002/2017JD028035>

567 Ma, N., & Szilagyi, J. (2019). The CR of evaporation: a calibration-free diagnostic and
568 benchmarking tool for large-scale terrestrial evapotranspiration modeling. *Water Resources*
569 *Research*, 55. <https://doi.org/10.1029/2019WR024867>

570 Ma, N., Szilagyi, J., Zhang, Y., & Liu, W. (2019). Complementary-relationship-based modeling
571 of terrestrial evapotranspiration across China during 1982-2012: Validations and spatiotemporal
572 analyses. *Journal of Geophysical Research-Atmospheres*, 124. <https://doi.org/2018JD029850>

573 Ma, N., Szilagyi, J., & Zhang, Y. (2021). Calibration-free complementary relationship estimates
574 terrestrial evapotranspiration globally. *Water Resources Research*, 57, e2021WR029691.
575 <https://doi.org/10.1029/2021WR029691>

576 Monteith, J. L. (1981). Evaporation and surface temperature: Evaporation and surface
577 temperature. *Quarterly Journal of the Royal Meteorological Society*, 107(451), 1-27.
578 <https://doi.org/10.1002/qj.49710745102>

579 Morton, F. I. (1983). Operational estimates of areal evapotranspiration and their significance to
580 the science and practice of hydrology. *Journal of Hydrology*, 66, 1-76.

581 Penman, H. L. (1948). Natural evaporation from open water, bare soil and grass. *Proceedings of*
582 *the Royal Society A: Mathematics, Physics and Engineering Sciences*, 193, 120-145.
583 <https://doi.org/10.1098/rspa.1948.0037>

584 Priestley, C. H. B., & Taylor, R. J. (1972). On the assessment of surface heat flux and
585 evaporation using large-scale parameters. *Monthly Weather Review*, 100(2), 81-92.

586 Qualls, R. J., & Crago, R. D. (2020). Graphical interpretation of wet surface evaporation
587 equations. *Water Resources Research*, 56, e2019WR026766.
588 <https://doi.org/10.1029/2019WR026766>

589 Schneider, U., Becker, A., Finger, P., Meyer-Christoffer, A., & Ziese, M. (2018). GPCP Full
590 data monthly product version 2018 at 0.25°: Monthly land-surface precipitation from rain-gauges
591 built on GTS-based and historical data.
592 https://doi.org/10.5676/DWD_GPCC/FD_M_V2018_025

593 Stull, R. B. (2000). *Meteorology for Scientists and Engineers*. Brooks/Cole, Pacific Grove, CA,
594 USA.

595 Szilagyi, J. (2014). Temperature corrections in the Priestley-Taylor equation of evaporation.
596 *Journal of Hydrology*, 519, 455-464. <https://doi.org/10.1016/j.jhydrol.2014.07.040>

597 Szilagyi, J. (2018). A calibration-free, robust estimation of monthly land surface
598 evapotranspiration rates for continental-scale hydrology. *Hydrology Research*, 49.
599 <https://doi.org/10.2166/nh.2017.078>

600 Szilagyi, J. (2021). On the thermodynamic foundations of the complementary relationship of
601 evaporation. *Journal of Hydrology*, 593, 125916. <https://doi.org/10.1016/j.jhydrol.2020.125916>

602 Szilagyi, J., & Jozsa, J. (2008). New findings about the Complementary Relationship-based
603 evaporation estimation methods. *Journal of Hydrology*, 354, 171-186.
604 <https://doi.org/10.1016/j.jhydrol.2008.03.008>

605 Szilagyi, J., Crago, R., & Qualls, R. (2017). A calibration-free formulation of the complementary
606 relationship of evaporation for continental-scale hydrology. *Journal of Geophysical Research-*
607 *Atmospheres*, 122, 264-278. <https://doi.org/10.1002/2016JD025611>

608 Szilagyi, J., Crago, R., & Ma, N. (2020). Dynamic scaling of the generalized complementary
609 relationship (GCR) improves long-term tendency estimates in land evaporation. *Advances in*
610 *Atmospheric Sciences*, 37 (9), 1–12. <https://doi.org/10.1007/s00376-020-0079-6>

611 Twine, T. E., Kustas, W. P., Norman, J. M., Cook, D. R., Houser, P. R., Meyers, T. P., Prueger,
612 J. H., Starks, P. J., & Wesely, M. L. (2000). Correcting eddy-covariance flux underestimates
613 over a grassland. *Agricultural and Forest Meteorology*, 103(3), 279-300.
614 [https://doi.org/10.1016/S0168-1923\(00\)00123-4](https://doi.org/10.1016/S0168-1923(00)00123-4)

615